Lab on a Chip

PAPER

View Article Online
View Journal | View Issue

Cite this: *Lab Chip*, 2016, **16**, 3576

Hydrodynamic trapping for rapid assembly and *in situ* electrical characterization of droplet interface bilayer arrays†

Mary-Anne Nguyen,[a] Bernadeta Srijanto,[b] C. Patrick Collier,[b] Scott T. Retterer[c] and Stephen A. Sarles*[a]

The droplet interface bilayer (DIB) is a modular technique for assembling planar lipid membranes between water droplets in oil. The DIB method thus provides a unique capability for developing digital, droplet-based membrane platforms for rapid membrane characterization, drug screening and ion channel recordings. This paper demonstrates a new, low-volume microfluidic system that automates droplet generation, sorting, and sequential trapping in designated locations to enable the rapid assembly of arrays of DIBs. The channel layout of the device is guided by an equivalent circuit model, which predicts that a serial arrangement of hydrodynamic DIB traps enables sequential droplet placement and minimizes the hydrodynamic pressure developed across filled traps to prevent squeeze-through of trapped droplets. Furthermore, the incorporation of thin-film electrodes fabricated *via* evaporation metal deposition onto the glass substrate beneath the channels allows for the first time *in situ*, simultaneous electrical interrogation of multiple DIBs within a sealed device. Combining electrical measurements with imaging enables measurements of membrane capacitance and resistance and bilayer area, and our data show that DIBs formed in different trap locations within the device exhibit similar sizes and transport properties. Simultaneous, single channel recordings of ion channel gating in multiple membranes are obtained when alamethicin peptides are incorporated into the captured droplets, qualifying the thin-film electrodes as a means for measuring stimuli-responsive functions of membrane-bound biomolecules. This novel microfluidic-electrophysiology platform provides a reproducible, high throughput method for performing electrical measurements to study transmembrane proteins and biomembranes in low-volume, droplet-based membranes.

Received 24th June 2016,
Accepted 1st August 2016

DOI: 10.1039/c6lc00810k

www.rsc.org/loc

Introduction

The droplet interface bilayer (DIB) is a highly versatile technique[1–3] for constructing model cell membranes (*i.e.* lipid bilayers) between low-volume lipid-coated aqueous droplets encased in oil (Fig. 1). DIB assemblies provide a suitable environment for studying many aspects of membrane transport including antimicrobial peptide or pore-forming protein insertion and gating.[1,2,4] DIB systems have also been employed recently to use biomolecular functionality for sensing,[5–7] actuation,[8] and energy conversion[9,10] applications.

There are several methods available for generating and arranging lipid-coated droplets to form DIBs. The most common DIB assembly method employs manual pipetting of aqueous volumes to form droplets, followed by positioning droplets to encourage contact-initiated bilayer formation. Examples of ways to arrange pipetted droplets include the use of micromanipulator(s) to push and pull droplets *via* wire-type electrodes,[3] rigid, solid substrates containing adjacent wells for droplet positioning,[2,11] mechanical force to control the compression of a solid substrate and regulate inter-droplet contact,[12] applied electrical fields to slide droplets across a dielectric surface,[13,14] and even magnetic fields to lift and place droplets containing magnetic species.[15,16]

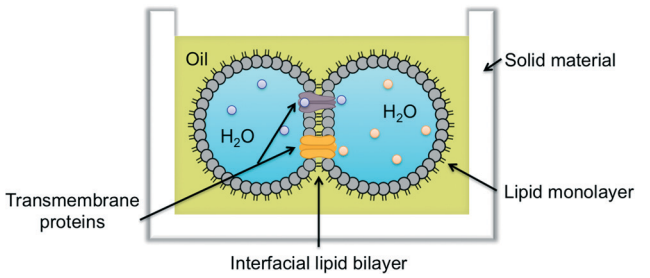

Fig. 1 Side view schematic of a droplet interface bilayer formed between two lipid encased aqueous droplets submerged in oil.

[a] *Department of Mechanical, Aerospace, and Biomedical Engineering, University of Tennessee, USA. E-mail: ssarles@utk.edu*
[b] *Oak Ridge National Laboratory, Center for Nanophase Materials Sciences, USA*
[c] *UT-Battelle, LLC, Biosciences and Center for Nanophase Materials Sciences, USA*
† Electronic supplementary information (ESI) available. See DOI: 10.1039/c6lc00810k

While many of these techniques enable precise control over droplet position and even bilayer area,[4,17–19] manually dispensing and arranging droplets is best suited for creating DIBs with droplets larger than 100 μm in diameter (≳50 nL) due to the minimum dispensing volume of a pipette (~50–100 nL) and the difficulties in individually manipulating small droplets.

Flowing oil and water through microfluidic junctions provides an alternative means to generate aqueous droplets in oil.[20–22] While there are multiple geometries for microfluidic droplet generators,[20,21] the droplet formation process is generally based on the relative flow rates of oil and water supplied to the device and on the dimensions of the channel(s), which typically range from 1 μm to several hundred micrometers in width and height. This approach is specifically well suited for generating continuous streams of low-volume (including fL and pL volumes) droplets. Once droplets are formed in a microchannel, hydrodynamic trapping can be employed to capture droplets from a moving stream and place them in stationary locations.[23–25] For instance, circular-shaped traps[26–29] and pillars/rails arrays[30–33] have been used to arrange lipid-coated water droplets to form DIBs within microfluidic devices.

Bilayer formation and membrane properties are often confirmed and quantified, respectively, in DIBs (as well as for other model membrane systems) using electrical measurements of membrane capacitance and resistance.[3,18,34,35] Electrophysiology measurements are also standard protocol for recording ion transport through transmembrane peptides and proteins.[3,29,36,37] DIBs formed with large droplets (*e.g.* ~1 mm diameter) allow for wire-type electrodes to be inserted into the droplets for applying voltage and measuring current across the interface. However, droplets formed in a microfluidic platform can be much smaller in size (*e.g.* from 2–350 μm diameter[20]) than ones that are manually dispensed and often remain within the sealed device, which complicates electrode access for electrical measurements.[29] As a result, imaging techniques have primarily been used thus far to confirm bilayer formation and quantify mass-transport across membranes for DIBs in microfluidic devices.[26,28,30–33]

Integrating electrodes into microfluidic platforms for membrane electrophysiology has received significant attention in recent years. For example, Behrends, *et al.* developed microfluidic, parallel patch-clamp systems with thin-film surface electrodes for enabling simultaneous electrophysiology of multiple cells suctioned at separate locations in the device.[38–40] Separately, thin film electrodes have been used in microfluidic devices to electrically interrogate suspended lipid bilayers (SLBs) formed across the pores of a dividing substrate[41–46] or between the walls of microfluidic channels.[47] While some of these platforms were connected to multi-channel current measurement devices that permit simultaneous measurements of multiple membranes,[43–46,48,49] others, including a study of a 2-DIB array using thin film electrodes, were paired with digital switching circuits to cycle a single-channel measurement device across multiple electrode pairs.[14,42,47]

Therefore while a few studies have included simultaneous measurements of multiple DIBs,[48,49] none has demonstrated this capability within a microfluidic device. To address this gap, we present a new microfluidic architecture that is capable of producing and routing low-volume aqueous droplets to predetermined locations for automated DIB formation and which features thin-film surface electrodes located beneath droplet pairs for enabling *in situ* electrical interrogation of multiple DIBs within the sealed device. A circuit-based modeling approach is employed to design and arrange hydrodynamic traps that are used for immobilizing droplets and enabling DIB formation at predetermined locations. Experiments performed on prototype devices fabricated based on model predictions demonstrate the ability to form multiple sets of DIBs within an enclosed device. By connecting the built-in electrodes to a multi-channel patch clamp amplifier, we show for the first time in a microfluidic device the ability to simultaneously assess bilayer capacitance during successive DIB formations and record stochastic, voltage-dependent ion channel gating in multiple membranes.

Resistive circuit model for direct trapping and droplet sorting

Our understanding of droplet behavior within a microfluidic device is guided by relating fluidic systems to electrical circuits. Using an electrical circuit analogy, a resistive flow model is developed to determine appropriate dimensions for the fluid channels used for droplet sorting and trapping as well as for designing the layout of a multi-trap array. In a single-phase laminar flow, the pressure difference along a section of a microchannel is equal to the product of the applied volumetric flow rate, Q, and the hydrodynamic resistance of the channel, R. The hydrodynamic resistance for Poiseulle flow in a rectangular channel[2,3] is given by

$$R = \frac{12\mu L}{h^3 w}\left[1 - \frac{192}{\pi^5}\times\frac{h}{w}\times\tanh\left(\frac{\pi w}{2h}\right)\right]^{-1} \quad (1)$$

where L, w, and h are the length, width, and height, respectively, of a particular segment of the channel, and μ is the viscosity of the carrier fluid (*i.e.* oil for a DIB system). Assuming that the presence of dispersed droplets in the oil does not significantly affect the relationship between pressure and applied flow rate, eqn (1) can be used to design channels of specific dimensions to dictate the flow resistance in regions of a device and thereby affect the course of droplet travel.

We seek to obtain a device that utilizes steady fluid flow to place trains of separated droplets into sequential hydrodynamic traps, which serve to position adjacent droplets close enough to enable spontaneous bilayer formation. A single hydrodynamic trap can be designed to accommodate two droplets to form one DIB (Fig. 2), or it can be configured to host more than two droplets to enable the formation of a linear

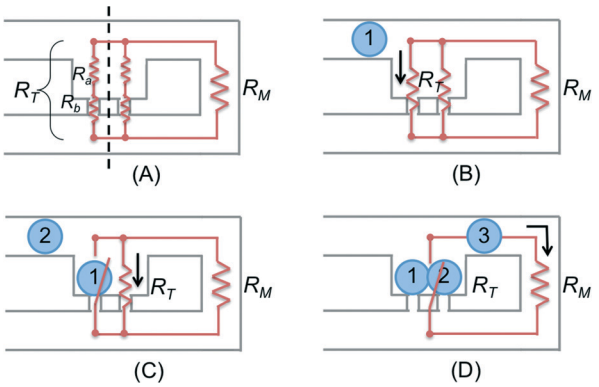

Fig. 2 Schematic of hydrodynamic flow resistances in a single, 2-droplet trap. (A) Diagram of an unfilled trap designed for two droplets, where each lane of the unfilled trap has an equivalent resistance of $R_a + R_b$. (B) Droplet 1 enters the trap when the total trap resistance, R_T, is less than resistance of the main channel, R_M. (C) Droplet 2 enters the open lane of the same trap if R_T through the remaining portion of the trap is still less than R_M. (D) R_T becomes greater than R_M once two droplets are trapped, causing following droplets to bypass the filled trap.

multi-membrane DIB series. In our device, a trap will consist of a rectangular compartment that resides adjacent to the main flow channel, which carries lipid-coated droplets in a stream of oil. Opposite entry from the main channel, each trap also features narrow exit channels, which we refer to as bleed valves.

The trap design and its ability to collect droplets carried in the main stream are thus based on the hydrodynamic resistance of the trap relative to that of the bypassing main channel. For instance, a droplet will prefer to enter an empty trap that has a hydrodynamic resistance, R_T, less than that of the resistance offered by bypassing the trap and flowing through the main channel, R_M. First, note that we approximate the hydrodynamic resistance of an n-droplet trap by dividing the trap into n-parallel lanes (from main channel to bleed valve) of equal hydrodynamic resistance (Fig. 2A). These lanes represent the contribution to total flow resistance as would be experienced by a droplet as it travels across each lane of the trap from the main chain to a bleed valve. The flow resistance of each lane in a trap is calculated by

$$R_T = R_a + R_b, \tag{2}$$

where R_a is the portion of lane resistance due to the rectangular body of the trap and R_b represents the contribution to lane resistance from the bleed value. In this way, the total resistance for an unfilled, two-droplet trap would be given by $R_T/2$, which is the parallel addition of two equal lane resistances. While a standard trap is designed to house two droplets for 1 DIB, the number of lanes in a trap can be expanded to capture more than two droplets to form multiple interfaces. This expansion affects the total hydrodynamic resistance of the empty trap. For example, the unfilled trap resistance is $R_T/3$ for a three-droplet trap.

When R_T is less than R_M, the first droplet in an incoming droplet train will divert from the main channel and come to rest in the hydrodynamic trap near one of the bleed valves (Fig. 2B). If the total flow resistance through the remaining lane(s) of the trap is still less than that offered by the main channel, a second droplet will also preferentially flow into the open half of the same trap (Fig. 2C). The bleed valves halt the droplets within the trap as long as the resulting pressure drop that develops across a droplet blocking a bleed valve does not cause the droplet to squeeze-through and escape. Specifically, the pressure drop across a filled trap must remain less than the Laplace pressure, ΔP_L, across the droplet residing at the entrance of a bleed valve, which can be calculated *via*

$$\Delta P_L = 2\gamma\left(\frac{1}{w_b} - \frac{1}{w_t}\right), \tag{3}$$

where, γ is interfacial tension of droplet–oil interface and w_b and w_t are widths of the bleed valve and trap, respectively.[23] Once a 2-droplet trap fills, the presence of droplets at the entry to all bleed valves causes the flow resistance to increase significantly. As a result, the third droplet in the train bypasses the filled trap, preferring to remain in the main channel, which now offers a relatively lower resistance to flow (Fig. 2D). Thus, an open trap behaves like a closed switch in an electrical circuit (with low resistance and high flow rate), while a filled trap acts like an open switch (with high resistance and low flow rate). This mechanism for droplet placement is known as direct trapping,[23] because the relatively lower trap resistance enables droplets to directly enter vacant traps and detour filled traps. Indirect trapping is associated with open traps that exhibit a higher relative resistance compared to the main channel.[23] For these, filling of traps occurs when droplets present in a section of the main channel past the trap momentarily increase its local resistance, thereby redirecting successive droplets into the open trap.

The concept of direct trapping is essential for automatically filling many traps in a device with multiple droplets for DIB array formation. However, because the hydrodynamic resistance offered by both the main channel and a trap depend on the connection of these sections to additional traps or channels located downstream, designing a device to operate in a direct trapping mode must consider the entire fluidic resistance of the device. This information is especially necessary for understanding how to configure arrays of traps such that large networks of DIBs can be efficiently and quickly assembled in a microfluidic device. Thus, we develop a resistive circuit model that enables calculation of fluid flow rates and pressure drops between channel intersections for characterizing the direct trapping performance of a multiple-trap device.

For this analysis, we consider three configurations of trap arrays that include both parallel and serial arrangements of traps within a network (Fig. 3A–C). In Model 1, the main channel connects the entrances to successive traps arranged in parallel before looping back to reconnect the outlets of

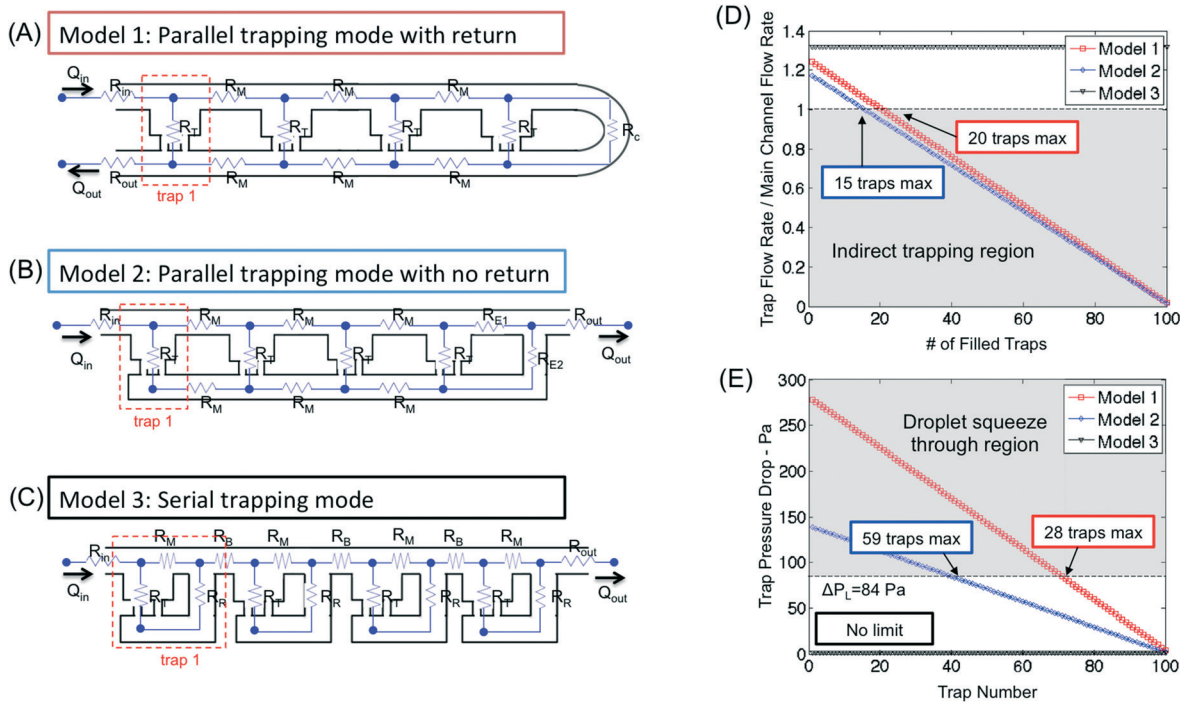

Fig. 3 Schematics and equivalent circuits for three trap array layouts: (A) Model 1 includes a main channel that returns to connect every trap's bleed valves; (B) Model 2 features a lower channel that reconnects to the upper main channel at the end of the array; and (C) Model 3 includes an individual return line for each trap. (D) Calculated flow rate ratio through an empty trap *versus* the main channel as a 100-trap system is being filled. The unshaded region identifies when traps fill *via* direct trapping, while the shaded region identifies those filled *via* indirect trapping. (E) Estimated pressure drop within a filled trap *versus* location in the array, where the shaded region identifies locations in the array where droplets would be squeezed through the bleed valves due to excessive pressure.

each trap before exiting the device—we refer to the main channel as "returning" to the traps before exit. The second model is similar to Model 1; however, there is no return path of the main channel. Instead a parallel channel that conducts between the exits of the traps and intersects the main channel at the end of the trap array is used to route excess oil flow away from the traps. Finally, Model 3 showcases a serial trap layout, where each trap has its own return path for excess oil that intersects the main channel prior to the next trap.

To enable sufficient comparisons of these layouts, values of channel resistances used in the modeling analysis are based on identical rectangular traps, each with a total width of 240 μm and a length of 130 μm, and using equal bleed valves that are 35 μm wide and 20 μm long. These dimensions reflect the approximate sizes need to capture a pair of 125 μm diameter droplets in a trap. Sections of main channel are assigned equal widths of 125 μm and all channels have a depth of 125 μm. These dimensions correspond to equivalent resistances of 770 Pa s μL^{-1} and 1.3×10^3 Pa s μL^{-1} for R_T and R_M, respectively.

To evaluate each layout, we write Kirchoff's Current law for fluid flow at each channel intersection in an array. This establishes a set of coupled equations as given by

$$[R]P = Q, \quad (4)$$

where $[R]$ represents a square coefficient matrix of reciprocal hydrodynamic resistances (*i.e.* conductance values) between nodes, P is a column vector of unknown absolute pressures at each node, and Q is a column vector of known applied flow rates. Analysis is performed on arrays of up to 100 traps by developing the appropriate form of eqn (4) for each of the three array types and by applying a fixed input flow rate, Q_1, at the intersection of the main channel and the entry to trap 1. Solving these matrix equations thus allows us to compute the pressure distribution in the array (*i.e.* analogous to the voltage at each node) and calculate for each trap in an array the ratio of fluid flow entering the trap to that which bypasses the trap, which allows us to determine if direct trapping occurs. These calculations are performed sequentially for a decreasing number of traps in an array to predict how changes in trapping mode and pressure distribution can arise from sequential trap filling. Recall that once a trap is filled, it acts like an open circuit, which thereby eliminates it from the circuit. Additional details regarding the general form of these matrix equations and sample MATLAB scripts for the three models are provided in section S1 of the ESI.†

The flow rate within each section of a multi-trap model is computed by dividing the difference in absolute pressure between nodes by the hydrodynamic resistance of that section. Fig. 3D shows the ratio of flow rate entering the first trap of a section of successive unfilled traps to the flow rate

bypassing that first trap. This calculation is performed sequentially by varying the number of filled traps in a 100-trap model. Therefore, the flow rate ratio reflects the preference of a droplet approaching the first unfilled trap to either enter the trap or bypass it. A ratio greater than one indicates direct trapping as marked by the unshaded region in Fig. 3D. Only Model 3 provides constant direct trapping during complete filling of the 100-trap array. This result is due to the fact that the pathway exiting each trap rejoins the main channel prior to the next trap, which effectively decouples the ratio of R_T to R_M of a trap from the remaining portion of the array. Said differently, only the local channel geometry affects the resistance ratio, which ensures direct trapping is maintained across all traps. Model 1 and Model 2 also exhibit a flow rate ratio greater than one for small numbers of filled traps. However their ratios of flow rates decrease steadily as traps fill, caused by an increase in effective trap resistance that results when the number of unfilled traps in the array decreases (*i.e.* fewer traps in parallel produces a higher effective resistance of flow through traps). Fig. 3D shows that the threshold for transitioning between direct and indirect trapping is 20 and 15 traps, respectively, for these two models.

The pressure drop across each trap is computed by determining the difference in absolute pressure between the entrance and exit nodes of the trap. This calculation is performed for all traps in a filled array to determine if droplet squeeze-through will occur (*i.e.* during filling of successive traps when the applied flow rate at the inlet is nonzero) for each model (Fig. 3E). Arrays of filled traps are considered specifically since this condition represents the highest absolute pressure a system can experience and corresponds to when droplets could be squeezed through the bleed valves. The following comparison is based on a filled array consisting of 100 equal traps, and the occurrence of squeeze-through is assessed when the pressure drop across a trap is higher than a Laplace pressure of 84 Pa (shown as the shaded region) determined using a droplet surface tension of 2 mN m^{-1} and trap and bleed valve widths of 130 μm and 35 μm, respectively.

This analysis shows that successive traps arranged in a parallel scheme (in Models 1 and 2) display linearly decreasing pressure drops with increasing trap number, where the first filled trap in a 100-trap array exhibits the highest pressure drop (275 Pa and 148 Pa, respectively) and the last filled trap exhibits the lowest pressure drop. Identifying where these two regressions cross the critical Laplace pressure of 84 Pa shows the maximum number (counting from the end of the series) of traps that can be configured in that way before squeeze-through occurs. For example, only the last 28 traps in Model 1 will not experience droplet squeeze-through the bleed valve—this result can be interpreted as a maximum of 28 traps arranged in parallel with a return (as shown by Model 1) can be assembled without squeeze-through occurring when all are filled. Model 2 exhibits a lower pressure profile, with the final 59 traps in the array being able to retain the captured droplets. However, in the serial model (Model 3), we find that the pressure drop across each trap in the series is equal (~1.5 Pa), which shows that the pressure across a filled trap is independent of the remaining number of filled traps, and far less than 84 Pa. Thus, while the absolute pressure at the inlet to a serial array does increase with increasing numbers of filled traps, the pressure across each trap is not large enough to cause squeeze-through. Therefore, based on the fact that direct trapping is maintained as traps are successively filled and that the pressure across filled traps will not cause squeeze-through, a microfluidic device with a serial trap layout is chosen to capture droplets and form DIBs in designated traps.

Production of droplets with uniform diameters and intra-droplet spacing is not instantaneous in a microfluidic device, often requiring several minutes of continuous injection to reach a steady state. Heterogeneous droplet production is problematic because hydrodynamic traps downstream can become filled with a variety of sizes and number of droplets, which complicates DIB formation and interrogation. Droplets much larger than the specified trap dimensions can also overfill the trap as well as clog the main channel, which disrupts the dynamics of droplet trapping downstream. Therefore, a pre-trap shunt is implemented to remove undesired droplets from the array prior to droplet trapping. The shunt is designed such that when the shunt outlet is open, the shunt offers a lower hydrodynamic resistance (R_{Shunt}) than that of the trap array ($R_{TrapArray}$), which causes droplets to exit the device *via* the shunt instead of filling the trap array (Fig. 4). Once droplets of desired size are obtained from the T-junction, the shunt outlet is manually sealed with tape, causing the droplet stream to now bypass the shunt and continue through the main channel to be trapped downstream.

Results and discussion

Resistance based droplet sorting

Aqueous droplets are generated at a T-junction, where the width of the main channel for the continuous oil phase is 125 μm and the minimum width of the dispersed phase channel (buffer) is 30 μm. All channels in the fabricated device have a depth of 125 μm. With these fixed geometries, we

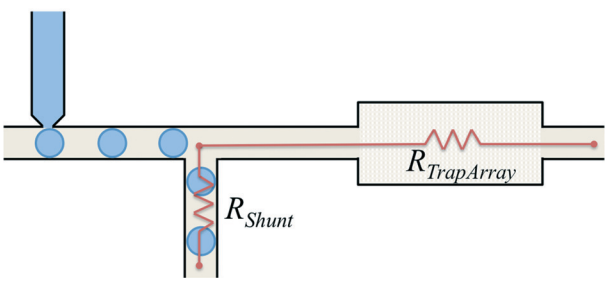

Fig. 4 Schematic of droplets entering the shunt when shunt resistance, R_{shunt}, is less than resistance of total trap array, $R_{TrapArray}$, downstream.

can vary the average droplet diameter produced at the T-junction from 70–125 μm by varying the relative oil and water flow rates (see Fig. S2†). Flow rates of 0.4–1 μL min^{-1} for oil and 0.05–0.5 μL min^{-1} for aqueous phase are used to produce 90–125 μm diameter droplets, which is the target droplet size for the trap dimensions. The transient time required for the device to produce stable droplet sizes from the T-junction following a change in the applied flow rates is approximately 5–10 minutes.

From the T-junction, the droplet stream continues through the main channel to a point where droplets can either enter the shunt channel or continue through the main channel to the trap array as shown in Fig. 5A. The fabricated shunt is 125 μm wide and 2.5 mm long, which yields a resistance of 4.2×10^3 Pa s μL^{-1} from the intersection to the outlet. This value is an order of magnitude less than that offered by smallest total downstream resistance created by the 16-trap array, which has a value of 4.3×10^4 Pa s μL^{-1}. Large droplets (*i.e.* slugs) are discarded through the outlet by keeping the shunt outlet open (Fig. 5B). The shunt outlet is then sealed with tape to enable trapping droplets that are similar diameter to the width of the main channel (Fig. 5C). Videos of droplet sorting are provided with the ESI.†

Hydrodynamic traps for droplet position and DIB formation

Following the results of our circuit analysis, we fabricated microchips containing serial arrangements of either 16 or 40 identical hydrodynamic traps (Fig. 5D). Like Model 3 in Fig. 3C, the fabricated device features individual traps arranged in series, where the return channel for each trap re-enters the main channel at the entrance to the next trap (*i.e.* the value of R_m between traps is zero). However in the fabricated device, the serially connected traps are arranged in a zig-zag pattern rather than a linear arrangement to position more traps in the viewing area of our microscope. Based on these trap dimensions, the fluidic resistance of a single lane of an open trap, R_T, is computed to be 770 Pa s μL^{-1}, *versus* a main channel resistance, R_M, of 1.1×10^3 Pa s μL^{-1}. Since $R_T < R_M$, the fabricated devices are expected to exhibit direct trapping. Fig. 6A–C confirms this behavior in a 16-trap microchip, by showing the sequence of filling events in which droplets enter traps sequentially. Additionally, we observe no droplet squeeze-through in either 16-trap or 40-trap devices, which confirms that the pressure drop across the traps remain less than the critical Laplace pressure of 84 Pa.

Microfluidic DIBs formed in this work are constructed from either glyceryl monooleate (GMO) lipids dissolved in the oil or 1,2-diphytanoyl-*sn-glycero*-3-phosphocholine (DPhPC) lipids incorporated as liposomes within the droplets. Both lipid types were found to yield stable DIB formation when the continuous phase is squalene, indicating that lipid monolayer assembly results in well-packed monolayers around the droplets. Spontaneous bilayer formation between neighboring lipid-coated droplets in a trap is identified by the emergence of a bright, planar connection between adhered droplets. For instance, the droplet pairs in the three bottom leftmost traps in Fig. 6A appear to have formed GMO bilayers, whereas the pair of droplets in the upper leftmost trap have not yet formed a bilayer since the dark outline of each droplet is still present. Successive images of the filling processing show that a droplet enters a trap every 1–2 seconds and DIBs form within 2–3 seconds of adjacent droplets landing in a trap. The entire capturing process takes less than 2 minutes to fill 16–40 traps. Further, images reveal that captured DIBs are stable within the device for up to 12 hours after assembly, and we observe very low rupture rates during or immediately after trap filling. Note that while a

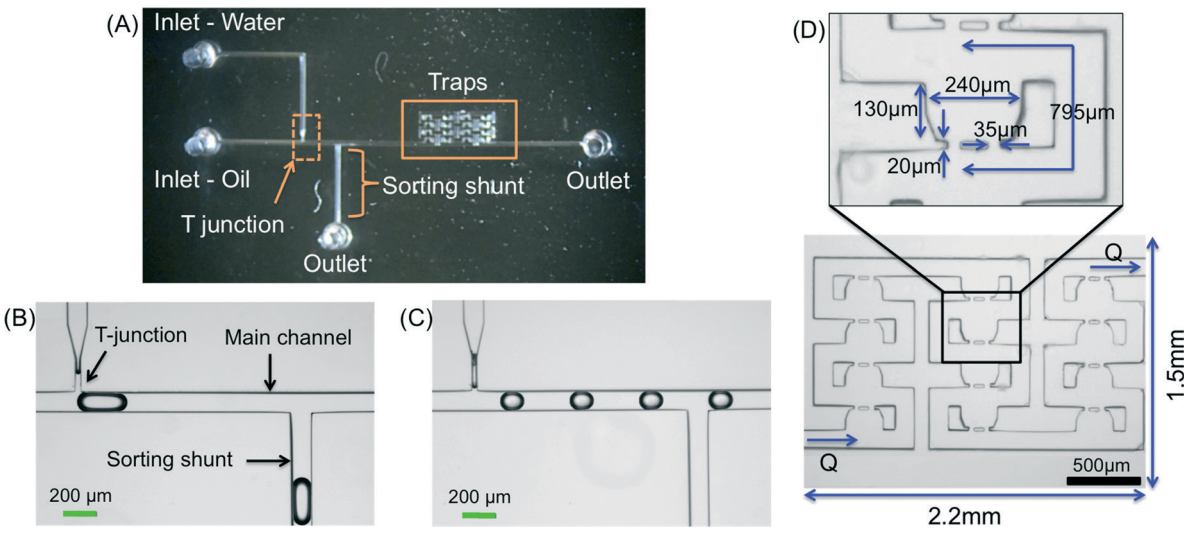

Fig. 5 (A) Top view of fabricated microchip. (B) Image of T-junction and droplets entering the shunt channel when outlet is open. (C) Droplets bypass the shunt channel when shunt channel outlet is sealed. (D) Layout of the serial hydrodynamic trap array. Each trap is designed for 125 μm diameter droplets, and the dimensions satisfy the resistance ratio for direct trapping.

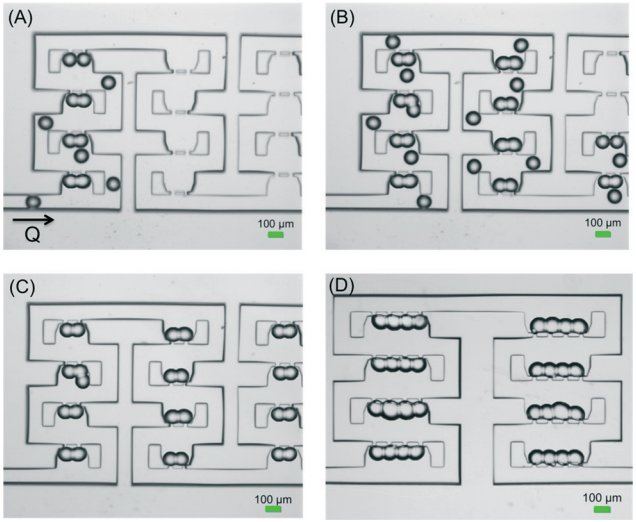

Fig. 6 (A–C) Image sequence of GMO-coated droplets being trapped sequentially in designated locations with no droplet squeeze-through. (D) Hydrodynamic traps are expanded to hold multi-bilayer networks such as four droplets in series to form three bilayers.

hydrodynamic pressure develops across each trap due to continued oil flow, this pressure is oriented parallel to the plane of the membrane. As a result, we do not believe continual oil flow to affect the stability of the membrane. However, any residual pressure-driven oil flow through the bleed valves of a filled-trap may also create a localized suction that pulls droplets together. Membrane rupture and droplet coalescence consistently occur after the 12 hour mark as a result of significant droplet shrinkage due to evaporation of water into the oil.[50,51]

Over the course of 10 droplet trapping and DIB formation experiments on 40-trap devices (n = 400 total traps analyzed), we observed that sequential droplet and DIB formation is highly reproducible. Specifically, the number of droplets captured in a trap matched the number of bleed valves (*e.g.* 2 droplets enters a trap with 2 bleed valves) in 95% of traps analyzed. The factors that led to a trap not containing the correct number of droplets include too low of an oil flow rate or too small of a droplet based on the trap dimensions. For instance, a third droplet may enter a two-droplet trap and form an additional bilayer if the oil flow rate is low ($<$0.4 μL min^{-1}) or if droplet diameters are $<$90 μm as seen in the second from the top, leftmost trap in Fig. 6B and C. These conditions, along with a small amount of oil still flowing through the bleed valves of a filled trap, can allow for a successive droplet to "dip" into an occupied trap and potentially form an additional bilayer. Once droplets were captured, successful and stable DIB formation occurred in 94% of traps. The success rate was lower than 100% due to the fact that neighboring droplets occasionally coalesce to form a large single droplet within a trap. When this occurs, the single volume can block only one bleed valve, which allows a new incoming droplet to be filtered out of the stream and captured to form a new membrane interface, or block both bleed valves, such that the trap does not attract a new droplet to form a DIB.

The serial arrangement of hydrodynamic traps maintains direct trapping even as we increase the number of droplets and bilayers in each trap. Fig. 6D shows an image of 8 traps in a 16-trap device where each trap has been expanded to capture more than two droplets to form serially connected DIB clusters. In this device, the main channel resistance is approximately 1.3 × 10^3 Pa s μL^{-1} compared to a single droplet lane trap resistance of 641 Pa s μL^{-1}. Therefore, droplets entering multi-DIB traps maintain the same direct trapping mechanism as before and are captured sequentially. Also, the pressure drop across a four-droplet trap (~22 Pa) is still less than the critical Laplace pressure required to cause squeeze-through (Table 1).

Electrical characterization of DIB arrays

Incorporating Ag/AgCl thin-film electrodes onto the glass surface (Fig. 7A) beneath the droplets provides a complementary method to imaging for characterizing DIBs and provides a more-efficient alternative to wire-type electrodes inserted into the microchannel.[29] Fig. 7B shows the fabricated electrode pattern design where each hydrodynamic trap has two electrode pads, with one designated as the sensing electrode and one connected to ground. A common ground electrode is shared between all eight pairs and is pseudo-colored red in the image. Electrode pad placement is determined from imaging the positions of trapped droplets observed in prior experiments. The total resistance of a single thin film electrode path is approximately 204 Ω from the droplet pad to connector pad where a cooper wire is soldered. We found the Ag/AgCl thin-film electrodes to be stable during experiments lasting up to 15 hours. During this time, there was no visual degradation when droplets containing 1 M NaCl reside on top of the electrodes.

Electrical measurements of adjoined droplets residing on a pair of electrode pads is used to characterize both the droplet–electrode interfaces as well as the membrane formed between droplets. The passive electrical properties of lipid bilayers are well established;[52,53] the membrane is represented by a resistor, R_b, in parallel with a capacitor, C_b. An additional series resistance, R_e, accounts for the electrolyte resistance of the aqueous phases on both side of the membrane (Fig. 7C). The resistance of a lipid bilayer is often greater than 1 GΩ, while the electrolyte resistance is typically on the order of 1 kΩ. If the droplet–electrode interface is resistive (*i.e.* the electrode makes direct contact with the aqueous interior of the droplet), then the equivalent circuit shown in Fig. 7C indicates that the dominant electrical impedance between two electrode pads is simply given by R_b and C_b. This condition implies that if the membrane fails (*i.e.* droplets coalesce), current flow between electrodes would increase significantly due to the lower value of R_e. However, if oil were to remain between the electrode pad and the droplet, then we expect a non-conductive, capacitance to exist at this interface (not

Table 1 Hydrodynamic resistances and pressures for empty and filled trap of 1 and 3 DIBs

Scenario	R_T (Pa s μL^{-1})	R_M (Pa s μL^{-1})	Q (μL min^{-1})	ΔP (Pa)
Empty trap – 1 DIB	770	1.1×10^3	1	7.6
Filled trap – 1 DIB	—	1.1×10^3	1	18.4
Empty trap – 3 DIB	641	1.3×10^3	1	7.17
Filled trap – 3 DIB	—	1.3×10^3	1	22

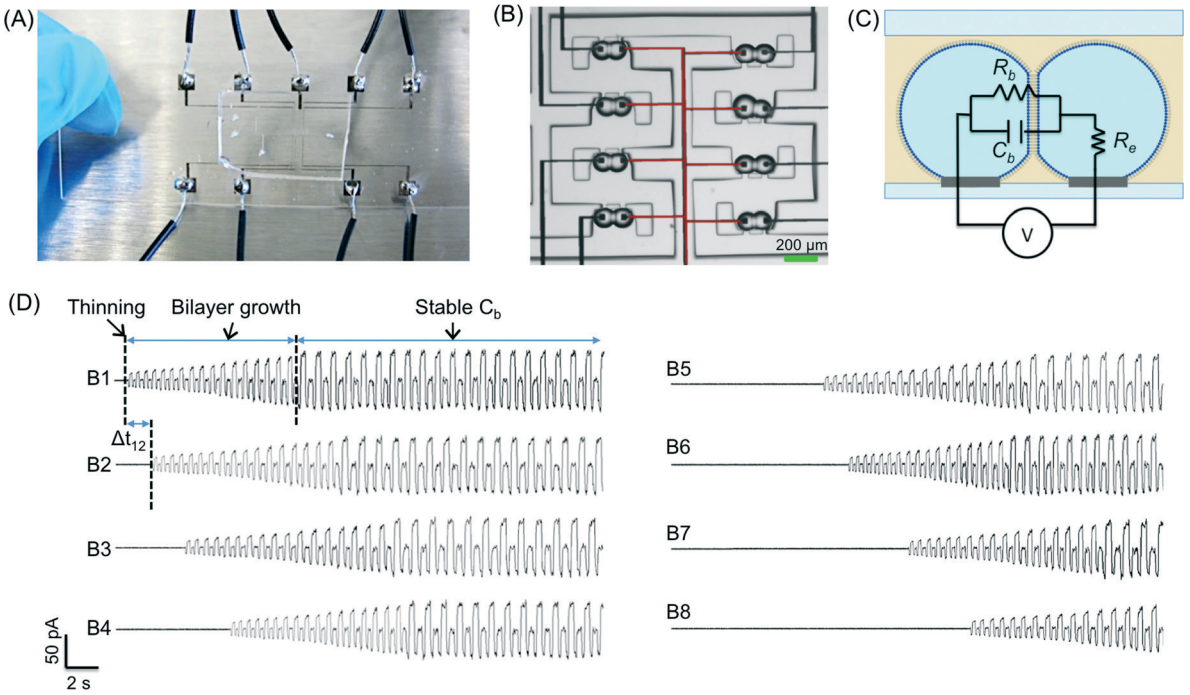

Fig. 7 Electrical characterization of microfluidic GMO DIBs: (A) Top view of microchip with thin-film electrodes and soldered wires. (B) Image of DIB residing on top of thin-film electrodes. Sensing electrodes are those on the outer side, while the shared ground electrode in the middle is pseudo colored red. (C) Equivalent electrical circuit of a DIB on top of Ag/AgCl thin-film electrodes. (D) Current measurements of 8 DIBs measured concurrently show increases in current amplitudes that correspond to the growth in bilayer capacitances during DIB formation. Currents are induced by a 40 mV, 50 Hz triangular waveform voltage.

shown in Fig. 7C). In this case, a dc current would remain low upon coalescence because of the capacitive contact with the droplets. In this study, we find that droplets form resistive connections with the Ag/AgCl electrode pads when *n*-decane or squalene are used as the oil, which is confirmed by a saturation of measured current when a single aqueous volume spans two electrodes (not shown). However, capacitive connections are established when hexadecane is used as the oil phase. Since electrophysiology of membranes typically requires a resistive connection between the electrodes and the electrolyte, we perform electrical measurements of microfluidic DIBs in squalene. Squalene is also preferred because it is not absorbed by PDMS.

Membrane formation in a DIB array is assessed electrically by simultaneously measuring the currents induced by an equal triangular waveform voltage applied between each electrode pair. When droplets are adjacent but not yet adhered, the presence of oil between them causes the induced current to be less than the background noise. As a bilayer forms, the increase in membrane capacitance causes a square waveform current to appear and then increase in amplitude. This sequence reflects the initial thinning and subsequent areal growth of the bilayer between droplets.[54] Fig. 7D shows electrical currents recorded during the spontaneous formation of 8 separate GMO DIBs (B1-B8). The 3–5 second time lag between onsets of successive DIB formation represents the time required for the next trap to fill and then a bilayer to form in that trap. Each membrane reaches a stable capacitance within ~10 seconds of the onset of thinning.

The raw current traces in Fig. 7D are used to compute the nominal capacitance and resistance of the bilayer as described elsewhere.[18] In parallel to electrical recordings, DIB area is calculated from the projected length of contact between droplets, which is measured from images of the droplet pair (such as those in Fig. 7B) using Image J software. This horizontal length of contact, or DIB lateral length,[19,55] is assumed to be equal to the circular diameter of the interface. Table 2 shows the steady-state membrane properties obtained

Table 2 Capacitance, resistance, area, specific capacitance, and normalized resistance for GMO DIBs obtained during three separate trials

	DIB #	Capacitance final (C_F) – pF	Resistance final (R_F) – GΩ	Area final (A_F) – μm^2	Specific capacitance (C_M) – μF cm^{-2}	Normalized resistance (R_N) – MΩ cm^2
Trial 1	Pair 1	11.0	8.1	1425	0.772	0.12
	Pair 2	11.0	8.8	1432	0.770	0.13
	Pair 3	11.0	8.0	1432	0.771	0.12
	Pair 4	11.0	8.1	1432	0.771	0.12
	Pair 5	11.0	8.1	1432	0.770	0.12
	Pair 6	11.1	8.8	1432	0.772	0.13
	Pair 7	11.0	8.2	1425	0.772	0.12
	Pair 8	11.1	8.1	1438	0.769	0.12
	Averages	11.0 ± 0.02	8.3 ± 0.3	1431 ± 4	0.771 ± 0.001	0.12 ± 0.01
Trial 2	Averages	16.7 ± 0.05	8.1 ± 0.2	2176 ± 4	0.769 ± 0.001	0.18 ± 0.004
Trial 3	Averages	12.9 ± 0.13	8.3 ± 0.4	1671 ± 9	0.773 ± 0.003	0.14 ± 0.01

from a single experiment for 8 GMO DIBs formed using ~100 μm diameter droplets. Nominal capacitance and membrane resistance for an 8-DIB array are plotted *versus* time in section S3 in the ESI.† From this experiment on 8 DIBs, the average membrane capacitance is 11.0 ± 0.02 pF and the average membrane resistance is 8.3 ± 0.3 GΩ. The image analysis shows that the average length of contact between droplets is 42.7 ± 2.3 μm, yielding an average circular area of 1431 ± 4 μm^2.

Specific membrane capacitance is computed for each DIB by dividing C_b by DIB area. The average specific capacitance from the 8 DIBs formed in the microchip is 0.771 ± 0.001 μF cm^{-2}, which is within the range of values of 0.75–0.81 μF cm^{-2} found in literature for GMO in squalene.[56] Multiplying R_m by area yields an average membrane resistivity of 0.12 ± 0.01 MΩ cm^2, which is comparable to typical liquid-supported lipid bilayers.[1,57]

The low standard deviation in membrane capacitance, resistance, and area within a set of 8 DIBs illustrates the uniformity of the droplets produced during a given experiment. However, multiple DIB array formation and electrical characterization experiments reveal that variations in average droplet size from one experiment to another are the primary cause for differences in nominal DIB properties between separate trials. For example, the average bilayer areas computed from two additional experiments (each using measurements from 8 GMO DIBs) are 2176 ± 4 μm^2 and 1671 ± 9 μm^2, respectively (Table 2). The droplet sizes for these trials were ~125 μm and ~110 μm in diameter, respectively. However, the average values of specific capacitance and membrane resistivity for DIBs formed in the three trials shown are very similar, which indicates that DIBs formed in the device exhibit consistent values of thickness and permeability from one experiment to the next. Tables providing individual bilayer properties from these additional trials are presented in section S4 of the ESI.†

Parallel single channel recordings

Alamethicin peptides, which exhibit concentration- and voltage-dependent pore formation in membranes,[58] are incorporated into the aqueous droplets to demonstrate parallel single-channel recordings in multiple DIBs using the thin-film electrodes. Voltage-induced gating is recorded with +170 mV applied equally across all 8 DPhPC DIBs; we found this level necessary to elicit pore formation for a final peptide concentration of 1 μM in the droplets. Simultaneous recordings of the resulting currents from all 8 DIBs are shown in Fig. 8A. For each membrane, we observe that the current stochastically fluctuates between discrete levels, which signifies transient pore formation and closure caused by peptides in the membrane.[59] Fig. 8B shows the calculated conductance *versus* time and Fig. 8C shows the corresponding histogram of these conductance levels for gating activity measured from one of the measurement channels (*i.e.* one of the DIBs). The ratios of alamethicin pore conductance relative to the subconductance level are found to be 1, 4.18, 8.73, and 14.07. These values are consistent with previous measurements of alamethicin activity in single DIBs.[35,57,60,61] However, this platform provides for the first time a reproducible and high throughput microfluidic method to simultaneously measure single-channel gating responses in multiple DIBs.

In the lipid-in[62] DIB technique used herein, liposomes contained within the droplets must fuse at the oil–water interface to form a monolayer prior to bilayer formation between droplets. Therefore while vesicle fusion after membrane formation is one way that alamethicin peptides reach the bilayer, it is highly likely that many alamethicin peptides are pre-associated with the monolayers coating the droplets prior to DIB formation. Our experiments with alamethicin consistently show immediate voltage-dependent ion channel formation after bilayer formation, which supports the notion that peptides are present on the membrane surface when the membrane forms.

Nonetheless, our microfluidic system to assemble and interrogate arrays of DIBs is equally well suited for lipid-out DIB formation, in which the lipids are incorporated outside of the droplets in the oil. Placing lipids in the oil ensures that the only bilayer membranes in the system are those that separate adjoined droplets. Further, incorporating the lipids in a separate phase from transmembrane proteins or other water-soluble species provides more control over the interactions between these species and the membrane[63,64] and enables easier application of osmotic gradients,[65,66] since the

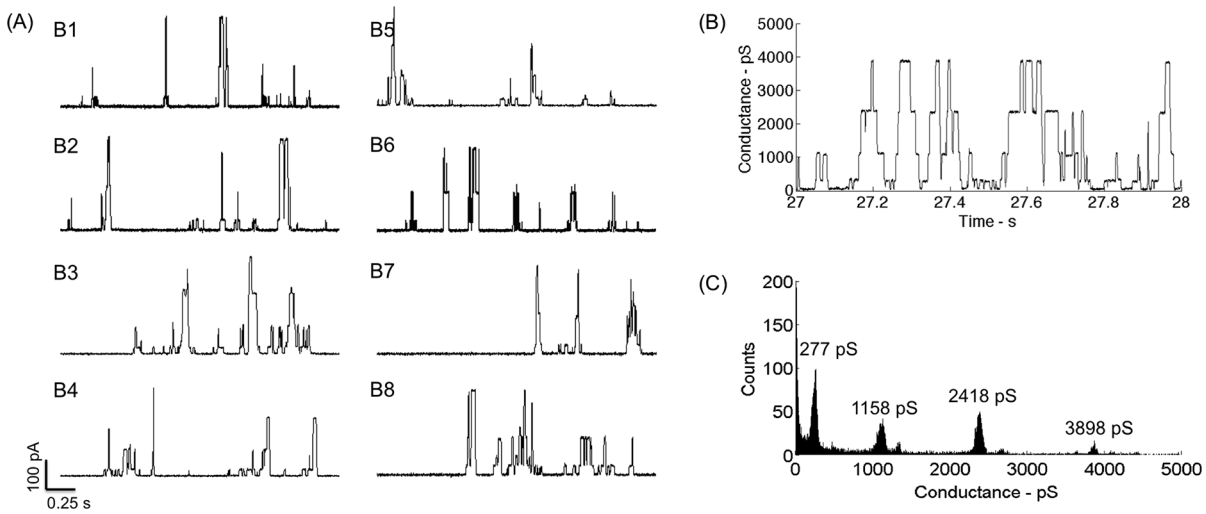

Fig. 8 (A) Simultaneous recordings of alamethicin gating activity in 8 DPhPC DIBs at a holding potential of +170 mV. (B) Conductance *versus* time of a single measurement channel. (C) Histogram of conductance values for alamethicin channels computed from the multiple gating events in (B).

interiors of the droplets do not contain an excess of liposomes or proteoliposomes.

Materials and methods

Materials

Sodium chloride (NaCl), 3-(*N*-morpholino)propanesulfonic acid (MOPS), sodium hydroxide (NaOH), ethanol, glyceryl monooleate (GMO), and squalene are acquired from Sigma Aldrich. Aqueous buffer is prepared by titrating 1 M NaCl, 10 mM MOPS stock solution with 0.5 M NaOH solution to achieve pH 7.4. GMO lipids are dissolved in squalene at a concentration of 2 mg mL^{-1}.

For alamethicin studies, lipid solution containing unilamellar liposomes is prepared with 2 mg mL^{-1} of 1,2-diphytanoyl-*sn-glycero*-3-phosphocholine (DPhPC, Avanti Polar Lipids) in 10 mM MOPS, 1 M NaCl, pH 7.4 buffer. Briefly, DPhPC lyophilized powder is dissolved in aqueous buffer solution followed by five freeze/thaw cycles. Then, the prepared stock solution is extruded through 100 nm pore polycarbonate membranes (Whatman) using an Avanti Mini Extruder to create unilamellar DPhPC liposome solution that is stored at 4 °C.

Alamethicin peptides (A.G. Scientific) from the fungus *Trichoderma viride* are dissolved in ethanol at 10 mg mL^{-1} and diluted with aqueous buffer to a final concentration of 2.5 mg mL^{-1} to create a stock solution that is stored at −20 °C. For DIB experiments with alamethicin, the stock solution is diluted to 25 μg mL^{-1} with buffer and then added to 2 mg mL^{-1} DPhPC liposome solution to achieve a final alamethicin concentration of 1 μM. Squalene is used at the organic phase in all experiments.

Device design and fabrication

A T-junction is used for droplet production. The incoming droplet stream is routed through microchannels and captured using series of hydrodynamic traps branching from the main channel. Each trap has an area designed to capture droplets serially with bleed valves that serve to direct the droplets into the vacant trap without allowing the droplets to escape after capture. Bleed valves are spaced such that the trapped droplets are close enough to connect to form a DIB. The device dimensions are tailored for 125 μm diameter droplets.

The microchips with 16 or 40 hydrodynamic traps are fabricated using standard photo- and soft-lithography techniques.[67] Briefly, a silicon wafer is spin-coated with photoresist and exposed to UV light through a chrome photomask using a photolithography aligner such that unmasked areas are cross-linked. Then, a deep reactive-ion etching process is employed to further etch the silicon wafer to a depth of 125 μm. After the master wafer is stripped of remaining photoresist and silanized to prevent adhesion during soft-lithography, uncured Sylgard 184 (Dow-Corning) PDMS (10 : 1 wt–wt ratio of base to curing agent) is poured over the wafer, degassed, and baked for at least 2 hours at 80 °C. Cured substrates are sliced and peeled off the master wafer. Inlet and outlet access holes are pierced using a 0.75 mm diameter biopsy punch. The PDMS substrate is bonded to a PDMS coated glass cover slide or a slide with deposited thin-film electrodes after an oxygen plasma treatment. The sealed devices are baked at 80 °C for at least 48 hours to create a hydrophobic environment.

Thin-film electrode fabrication

Electrodes are placed strategically such that each pad is directly under the trapped droplet. Similar to the microfluidic fabrication, a chrome photomask with the desired electrodes design is developed followed by photolithography with a glass wafer (Borofloat). A single electrode pathway includes a

30 × 30 μm droplet pad with leads extending in width increments connecting to a large 3 × 3 mm pad.

A dual gun electron beam evaporation chamber is used to deposit 10 nm adhesive layer of chrome and 300 nm of silver onto the glass wafer. Next, lift-off in acetone and isopropyl alcohol is performed to remove unattached metal. Prior to bonding with PDMS microchannels, bleach is pipetted onto the 30 × 30 μm electrode pads to form silver–silver chloride reversible electrodes. Chloride exposure is limited to less than 30 seconds to prevent over-bleaching. Then, the electrodes are thoroughly washed with deionized water. Microchips undergo plasma oxidation, bonded to PDMS, and baked at 80 °C for at least 48 hours. Then, silver wire is soldered onto the 3 × 3 mm pads in order to connect to the patch clamp amplifier.

Device operation

A dual syringe pump (Gemini 88, KD Scientific) is used to control the flow rates of the oil and water injections. PTFE tubing and 23 gage blunt stainless steel needles are used to connect syringes to the inlet ports of a microfluidic device. Images are obtained using a CCD camera (QImaging QIClick) connected to an inverted microscope (Olympus IX51). The device is also reusable and can be cleared *via* simple oil backwashed (see ESI† video of device flushing) through the outlet.

Electrical recordings

Electrical currents through lipid bilayers are monitored using an 8-channel patch clamp amplifier (Triton, Tecella LLC) and TecellaLab software to digitally control the applied voltage to the sensing electrode and measure the induced currents in the network. Each electrode is connected to a separate measurement channel on the amplifier. A picture of a device connected to the amplifier is shown in Fig. S5 in the ESI.† A triangular voltage waveform (40 mV, 50 Hz) is applied as needed on independent electrodes to monitor bilayer capacitance. Measured current is sampled at either 2 kHz for bilayer characterization measurements or 20 kHz for alamethicin gating measurements, filtered at 1 kHz using a low-pass filter, and digitized using 16-bit A/D conversion within the Triton. Local shielding with aluminum foil around the wired electrodes attached to the amplifier is used to reduce the noise. The calculated RMS noise in all experiments is less than ±10 pA, and we observe that the noise does not increase when the syringe pump is running and solution is flowing through the channels.

Conclusions

In this work, we designed and fabricated microfluidic devices developed to generate, sort, and trap droplets to form DIBs in designated traps. Specifically, hydrodynamic traps were designed using an equivalent circuit model to capture two, three, or four droplets to form either single bilayers or serially connected multi-DIB clusters in each trap. Through the circuit modeling analysis, we were able to design multiple-trap arrays that enable sequential droplet trapping and subsequent DIB formation between multiple pairs of droplets in a single device. The chosen serial configuration provides a constant, low-pressure drop across each filled trap, which is far less than the Laplace pressure across a droplet. Therefore, captured droplets are retained and are not pushed through the bleed valves after trapping. Trapping order will be especially important in future work, where captured droplets of alternating compositions are desired. In contrast, our analysis of multi-trap arrays that feature traps arranged in a parallel fashion did not fulfill the maximum pressure and direct trapping criteria, which placed limits on the number of traps that could be included within a device. Hence, these designs were not fabricated.

For the first time to our knowledge, we demonstrated the incorporation of thin-film electrodes and *in situ* electrical interrogation of multiple DIBs within an enclosed device. We used these conductive traces to simultaneously apply a voltage stimulus and measure the resulting currents through as many as 8 DIBs. Combined electrical and optical access allowed for measurements of membrane capacitance, resistance, and bilayer area for each DIB, and our experiments revealed that arrays of DIBs formed from a droplet stream exhibit consistent sizes and values of membrane resistivity. Also, parallel single channel recordings of alamethicin peptides were obtained *via* the thin-film electrodes in 8 DIBs at once. This capability for simultaneous electrical measurement in multiple DIBs supports the use of microfluidics and DIBs for high-throughput, low-volume electrophysiology experiments related to studying proteins, performing biosensing, and conducting drug-screening assays.

Acknowledgements

The authors would like to acknowledge funding from the Air Force Office of Scientific Research Basic Research Initiative Grant number FA9550-12-1-0464. Device fabrication was conducted at the Center for Nanophase Materials Sciences, which is a DOE Office of Science User Facility. Also, the authors would like to acknowledge Dale Hensley for assistance with microfabrication and Dr. Yoke Tanaka at Tecella, LLC for assistance in configuring the Triton amplifier for multi-channel measurements.

References

1 H. Bayley, B. Cronin, A. Heron, M. A. Holden, W. L. Hwang, R. Syeda, J. Thompson and M. Wallace, *Mol. BioSyst.*, 2008, **4**, 1191–1208.
2 K. Funakoshi, H. Suzuki and S. Takeuchi, *Anal. Chem.*, 2006, **78**, 8169–8174.
3 M. A. Holden, D. Needham and H. Bayley, *J. Am. Chem. Soc.*, 2007, **129**, 8650–8655.
4 S. A. Sarles and D. J. Leo, *Anal. Chem.*, 2010, **82**, 959–966.

5 S. A. Sarles, J. D. W. Madden and D. J. Leo, *Soft Matter*, 2011, **7**, 4644.
6 H. Bayley and P. S. Cremer, *Nature*, 2001, **413**, 226–230.
7 E. Sackmann, *Science*, 1996, **271**, 43–48.
8 V. B. Sundaresan, C. Homison, L. M. Weiland and D. J. Leo, *Sens. Actuators, B*, 2007, **123**, 685–695.
9 J. Xu, T. K. Vanderlick and D. A. LaVan, *Int. J. Photoenergy*, 2012, **2012**, 1–10.
10 J. Xu, F. J. Sigworth and D. A. LaVan, *Adv. Mater.*, 2010, **22**, 120–127.
11 S. A. Sarles and D. J. Leo, *Lab Chip*, 2010, **10**, 710–717.
12 S. A. Sarles and D. J. Leo, *Anal. Chem.*, 2010, **82**, 959–966.
13 S. Aghdaei, M. E. Sandison, M. Zagnoni, N. G. Green and H. Morgan, *Lab Chip*, 2008, **8**, 1617–1620.
14 J. L. Poulos, W. C. Nelson, T. J. Jeon, C. J. Kim and J. J. Schmidt, *Appl. Phys. Lett.*, 2009, **95**, 013706.
15 T. Wauer, H. Gerlach, S. Mantri, J. Hill, H. Bayley and K. T. Sapra, *ACS Nano*, 2013, **8**, 771–779.
16 K. Brahmbhatt, W. Zhao, Z. Deng, L. Mao and E. Freeman, presented in part at the *ASME 2015, Smart Materials, Adaptive Structures and Intelligent Systems*, Colorado Springs, CO, 2015.
17 L. C. M. Gross, O. K. Castell and M. I. Wallace, *Nano Lett.*, 2011, **11**, 3324–3328.
18 L. C. M. Gross, A. J. Heron, S. C. Baca and M. I. Wallace, *Langmuir*, 2011, **27**, 14335–14342.
19 G. J. Taylor, G. A. Venkatesan, C. P. Collier and S. A. Sarles, *Soft Matter*, 2015, **11**, 7592–7605.
20 R. Seemann, M. Brinkmann, T. Pfohl and S. Herminghaus, *Rep. Prog. Phys.*, 2012, **75**, 016601.
21 S. Y. Teh, R. Lin, L. H. Hung and A. P. Lee, *Lab Chip*, 2008, **8**, 198–220.
22 G. F. Christopher and S. L. Anna, *J. Phys. D: Appl. Phys.*, 2007, **40**, R319–R336.
23 S. S. Bithi and S. A. Vanapalli, *Biomicrofluidics*, 2010, **4**, 44110.
24 V. Labrot, M. Schindler, P. Guillot, A. Colin and M. Joanicot, *Biomicrofluidics*, 2009, **3**, 12804.
25 W. H. Tan and S. Takeuchi, *Proc. Natl. Acad. Sci. U. S. A.*, 2007, **104**, 1146–1151.
26 Y. Bai, X. He, D. Liu, S. N. Patil, D. Bratton, A. Huebner, F. Hollfelder, C. Abell and W. T. Huck, *Lab Chip*, 2010, **10**, 1281–1285.
27 M.-A. Nguyen and S. A. Sarles, presented in part at the *ASME 2014, Smart Materials, Adaptive Structures and Intelligent Systems*, Newport, RI, 2014.
28 T. Teshima, H. Ishihara, K. Iwai, A. Adachia and S. Takeuchi, *Lab Chip*, 2010, **10**, 2443–2448.
29 M. A. Czekalska, T. S. Kaminski, S. Jakiela, K. T. Sapra, H. Bayley and P. Garstecki, *Lab Chip*, 2015, **15**, 541–548.
30 P. H. King, G. Jones, H. Morgan, M. R. de Planque and K. P. Zauner, *Lab Chip*, 2014, **14**, 722–729.
31 M. Zagnoni and J. M. Cooper, *Lab Chip*, 2010, **10**, 3069–3073.
32 T. Nisisako, S. A. Portonovo and J. J. Schmidt, *Analyst*, 2013, **138**, 6793–6800.
33 P. Carreras, Y. Elani, R. V. Law, N. J. Brooks, J. M. Seddon and O. Ces, *Biomicrofluidics*, 2015, **9**, 064121.
34 W. L. Hwang, M. A. Holden, S. White and H. Bayley, *J. Am. Chem. Soc.*, 2007, **129**, 11854–11864.
35 S. A. Sarles and D. J. Leo, *J. Intell. Mater. Syst. Struct.*, 2009, **20**, 1233–1247.
36 H. Bayley, B. Cronin, A. Heron, M. A. Holden, W. L. Hwang, R. Syeda, J. Thompson and M. Wallace, *Mol. BioSyst.*, 2008, **4**, 1191–1208.
37 G. J. Taylor and S. A. Sarles, *Langmuir*, 2015, **31**, 325–337.
38 N. Fertig, R. H. Blick and J. C. Behrends, *Biophys. J.*, 2002, **82**, 3056–3062.
39 N. Fertig, M. Klau, M. George, R. H. Blick and J. C. Behrends, *Appl. Phys. Lett.*, 2002, **81**, 4865–4867.
40 A. Brüggemann, S. Stoelzle, M. George, J. C. Behrends and N. Fertig, *Small*, 2006, **2**, 840–846.
41 B. Le Pioufle, H. Suzuki, K. V. Tabata, H. Noji and S. Takeuchi, *Anal. Chem.*, 2008, **80**, 328–332.
42 M. Zagnoni, M. E. Sandison and H. Morgan, *Biosens. Bioelectron.*, 2009, **24**, 1235–1240.
43 A. Hirano-Iwata, T. Nasu, A. Oshima, Y. Kimura and M. Niwano, *Appl. Phys. Lett.*, 2012, **101**, 023702.
44 S. C. Saha, F. Thei, M. R. R. de Planque and H. Morgan, *Sens. Actuators, B*, 2014, **199**, 76–82.
45 S. C. Saha, A. J. Henderson, A. M. Powl, B. A. Wallace, M. R. R. de Planque and H. Morgan, *PLoS One*, 2015, **10**, e0131286.
46 G. Baaken, N. Ankri, A.-K. Schuler, J. Rühe and J. C. Behrends, *ACS Nano*, 2011, **5**, 8080–8088.
47 J. S. Shim, J. Geng, C. H. Ahn and P. Guo, *Biomed. Microdevices*, 2012, **14**, 921–928.
48 R. Kawano, Y. Tsuji, K. Sato, T. Osaki, K. Kamiya, M. Hirano, T. Ide, N. Miki and S. Takeuchi, *Sci. Rep.*, 2013, **3**, 1995.
49 Y. Tsuji, R. Kawano, T. Osaki, K. Kamiya, N. Miki and S. Takeuchi, *Anal. Chem.*, 2013, **85**, 10913–10919.
50 P. Mruetusatorn, J. B. Boreyko, G. A. Venkatesan, S. A. Sarles, D. G. Hayes and C. P. Collier, *Soft Matter*, 2014, **10**, 2530–2538.
51 J. B. Boreyko, P. Mruetusatorn, S. A. Sarles, S. T. Retterer and C. P. Collier, *J. Am. Chem. Soc.*, 2013, **135**, 5545–5548.
52 M. Montal and P. Mueller, *Proc. Natl. Acad. Sci. U. S. A.*, 1972, **69**, 3561–3566.
53 G. Wiegand, N. Arribas-Layton, H. Hillebrandt, E. Sackmann and P. Wagner, *J. Phys. Chem. B*, 2002, **106**, 4245–4254.
54 N. Tamaddoni, G. Taylor, T. Hepburn, S. Michael Kilbey and S. A. Sarles, *Soft Matter*, 2016, **12**, 5096–5109.
55 S. Punnamaraju and A. J. Steckl, *Langmuir*, 2011, **27**, 618–626.
56 S. H. White, *Biophys. J.*, 1978, **23**, 337–347.
57 S. A. Sarles and D. J. Leo, *Lab Chip*, 2010, **10**, 710–717.
58 I. Vodyanoy, J. E. Hall and T. M. Balasubramanian, *Biophys. J.*, 1983, **42**, 71–82.
59 L. G. Gordon and D. A. Haydon, *Biochim. Biophys. Acta*, 1976, **436**, 541–556.
60 J. B. Boreyko, G. Polizos, P. G. Datskos, S. A. Sarles and C. P. Collier, *Proc. Natl. Acad. Sci. U. S. A.*, 2014, **111**, 7588–7593.
61 G. J. Taylor and S. A. Sarles, *Langmuir*, 2015, **31**, 325–337.

62 W. L. Hwang, M. Chen, B. Cronin, M. A. Holden and H. Bayley, *J. Am. Chem. Soc.*, 2008, **130**, 5878–5879.
63 T. Nisisako, S. A. Portonovo and J. J. Schmidt, *Analyst*, 2013, **138**, 6793–6800.
64 A. Fischer, M. A. Holden, B. L. Pentelute and R. J. Collier, *Proc. Natl. Acad. Sci. U. S. A.*, 2011, **108**, 16577–16581.
65 Z. Michalak, D. Fartash, N. Haque and S. Lee, *CrystEngComm*, 2012, **14**, 7865–7868.
66 Z. Michalak, M. Muzzio, P. J. Milianta, R. Giacomini and S. Lee, *Langmuir*, 2013, **29**, 15919–15925.
67 J. C. McDonald and G. M. Whitesides, *Acc. Chem. Res.*, 2002, **35**, 491–499.